

A Frequency-Domain Linear ADR-Based Speed Control in Saddle-Shaped Model Predictive Current Control for PMSM

Yao Wei, Yanjun Wei, Yening Sun, Hanhong Qi, Mengyuan Li

*College of Electrical Engineering, Yanshan University, Qinhuangdao 066004 China
(Tel: 86-335-8058471, e-mail: weiyao@stumail.ysu.edu.cn, yjwei@ysu.edu.cn, sunyening@stumail.ysu.edu.cn, hhqi@ysu.edu.cn, 253424371@outlook.com).*

Abstract: A Linear-Active-Disturbance-Rejection-based Saddle-Shaped Model Predictive Current Control (LADR-SS-MPCC) strategy is proposed in this paper for a Permanent Magnet Synchronous Motor (PMSM) driving system. In the proposed method, a Linear-Active-Disturbance-Rejection-based (LADR-) structure compensates the unknown disturbances including predictive current errors and load torque fluctuations. Combined with the frequency-domain method of proportional-integral (PI) controller, the parameter sensitivities of Model Predictive Current Control (MPCC) and tuning method of the LADR-structure are analyzed in detail, and the influence and implementation of saddle-shaped and inserted harmonic waveforms for MPCC are also presented to improving current harmonics. Compared with the Proportional-integral MPCC (PI-MPCC) and the conventional LADR-MPCC strategies, the advantages including dynamics, robustness and stator current harmonic amplitudes are demonstrated by simulation and experimental results.

Keywords: PMSM, model predictive control, predictive error, parameter mismatch.

1. INTRODUCTION

PMSM is widely used in industry, such as 3-D printer, industry robot and lathe, because its advantages including high efficient, power density and torque-ampere ratio and low weight and volume. Model predictive control (MPC) is frequently applied in the power electronics and motor drives realms, and highlighted by the researchers and engineers in recent years due to its flexible design principle, less tuning parameters and fast dynamic response (Z. Zhang et al., 2017; T. Englert et al., 2018; T. Geyer, 2016; J. Rodriguez et al., 2012). MPC can be divided into two categories, including continuous control set MPC (CCS-MPC) and finite control set MPC (FCS-MPC) (F. Wang et al., 2017). CCS-MPC obtains a group of continuous variable voltage vector functions by solving an optimization problem, and generates a group of driving signals by the space vector pulse-width modulation (SVPWM) (Y. Wei et al., 2020; T. Geyer, 2013). FCS-MPC selects the optimal voltage vector by means of exhaustion to realize objectives in the cost function, and corresponds with characteristics of various converters with discrete-time variable switching frequency (C. Zheng et al., 2020).

Considering that the parameter values may vary in some systems while in other cases it is difficult to get a precise value of the parameter, one problem of the FCS-MPC is parameter robustness. The parameters of the motor such as stator resistances, inductions and magnet fluxes are always affected by environment temperature, operating states and magnetic circuit nonlinearity et al (T. Sun et al., 2020; Z. Zou et al., 2019). Based on the analysis of the predictive error of FCS-MPCC for a two-level inverter in (B. Wang et al. 2017),

the predictive torque errors are analysed under parameter mismatches, and torque errors and ripples are reduced by a torque correction mechanism (S. Siami et al., 2017). The parameter sensitivities of the MPCC are analysed, and the predictive currents are modified twice to suppress mismatches and predictive errors (X. Yuan et al., 2020).

Moreover, excepting some parameter identification methods to ensure parameter accuracy (Q. Wang et al., 2020), the predictive error caused by mismatched parameters can be regarded as a disturbance and observed by an observer such as the second-order sliding-mode disturbance observer, the high-gain observer and the error state observer (ESO) (B. Wang et al., 2018; L. Yan et al., 2020; M. Zareian et al., 2020; M. Habibulah et al., 2017). ESO and state error feedback-control-law (SEF) can be combined as an active-disturbance-rejection-based (ADR-) structure to replace the PI controller of speed-loop in the Proportional-integral model predictive torque control (PI-MPTC) and enhance compensation for predictive torque error (F. Wang et al., 2019). The parameters of ADR-structure have difficult tuning processes which need to be obtained based on a large number of simulation and experimental results because of two nonlinear functions and difficult structure. A LADR-structure makes the parameters relating to the controller bandwidth and the number of parameters is decreased by adjusting locations of the pole/zero points (J. Li et al., 2017; C. Liu et al., 2020).

For the predictive current error caused by parameter mismatches, a LADR-SS-MPCC for PMSM drives is proposed in this paper to compensate for predictive current error and decrease the amplitudes of harmonics by inserted and saddle-shaped waves based on the continuous control set

model predictive current control (CCS-MPCC). The influence of mismatched parameters on predictive current error is studied, and the basic principle and the advantages of LADR-SS-MPCC are analysed and demonstrated by the simulation and experimental results compared with the LADR-MPCC and PI-MPCC strategies.

The rest of this paper is organized as follows. Section II introduces the mathematical model of PMSM and the MPCC strategy. Section III introduces the proposed LADR-SS-MPCC and its implementation method. Section IV and V make a detailed comparison of the proposed method, LADR-MPCC and PI-MPCC by simulations and experiments. Finally, Section VI concludes this paper.

2. PMSM MODEL AND MPCC

2.1 Discrete-time Model of PMSM

The continuous-time functions including stator voltage u_s , stator flux linkage ψ_s and electromagnetic torque T_e on the dq coordinate can be expressed as:

$$\begin{cases} u_{sd} = R_s i_{sd} + L_s \frac{di_{sd}}{dt} - L_s \omega_r i_{sq} \\ u_{sq} = R_s i_{sq} + L_s \frac{di_{sq}}{dt} + L_s \omega_r i_{sd} + j\psi_m \omega_r \end{cases} \quad (1)$$

$$\begin{cases} \psi_{sd} = L_s i_{sd} + \psi_m \\ \psi_{sq} = L_s i_{sq} \end{cases} \quad (2)$$

$$T_e = \frac{3}{2} p \psi_m i_{sq} \quad (3)$$

where R_s is the stator resistance, L_s is the stator induction satisfying $L_{sd} = L_{sq} = L_s$ for surface PMSM, ω_r is the electrical angular frequency, ψ_m is the flux magnitude due to the rotor magnets and p is the number of pole pairs of the machine. The subscripts d and q denote the components on the d-axis or q-axis. The rotor dynamics can be described by the following expression:

$$\frac{d\omega_r}{dt} = \frac{p}{J} (T_e - T_L) - \frac{B}{J} \omega_r \quad (4)$$

where J is the rotor inertia, B is the friction coefficient and T_L is the load torque.

Combining (1) - (4), the Forward Euler interpolation method is applied to discrete model with sampling period T_s , and the predictive variables at time $k+1$ are also obtained as follows:

$$i_{sd}(k+1) = \left(1 - \frac{R_s T_s}{L_s}\right) i_{sd}(k) + T_s \omega_r i_{sq}(k) + \frac{T_s}{L_s} u_{sd} \quad (5)$$

$$i_{sq}(k+1) = \left(1 - \frac{R_s T_s}{L_s}\right) i_{sq}(k) - T_s \omega_r i_{sd}(k) - \psi_m \omega_r T_s + \frac{T_s}{L_s} u_{sq} \quad (6)$$

2.2 MPCC Strategy

The controlled objectives of MPCC include torque current reference tracking and torque by ampere optimization. These objectives can be expressed as the following cost function:

$$G = (i_{sd}(k+1))^2 + (i_{sq}(k+1) - i_{sq}^*)^2 \quad (7)$$

where i_{sq}^* is the reference of q-axis stator current. The first term represents the minimization of the reactive power, allowing the torque by ampere optimization, and the second term is defined for tracking the reference signal.

Expressing the cost function partial derivatives for the stator voltages, the partial derivative functions are defined equalling to zero and expressed as:

$$\frac{dG}{du_{sd}} = \frac{2T_s}{L_s} \left[\left(1 - \frac{R_s T_s}{L_s}\right) i_{sd}(k) + T_s \omega_r(k) i_{sq}(k) + \frac{T_s}{L_s} u_{sd} \right] = 0 \quad (8)$$

$$\frac{dG}{du_{sq}} = \frac{2T_s}{L_s} \left[\left(1 - \frac{R_s T_s}{L_s}\right) i_{sq}(k) - T_s \omega_r(k) i_{sd}(k) \right. \quad (9)$$

$$\left. - \psi_m \omega_r(k) T_s + \frac{T_s}{L_s} u_{sq} - i_{sq}^* \right] = 0$$

, and a group of voltage functions are obtained to solve the predictive stator voltages:

$$u_{sd} = \left(R_s - \frac{L_s}{T_s} \right) i_{sd}(k) - L_s \omega_r(k) i_{sq}(k) \quad (10)$$

$$u_{sq} = \left(R_s - \frac{L_s}{T_s} \right) i_{sq}(k) + L_s \omega_r(k) i_{sd}(k) + L_s \psi_m \omega_r(k) + \frac{L_s}{T_s} i_{sq}^* \quad (11)$$

2.3 Parameter Mismatch and Predictive Current Error

Assuming $i_s(k)$ and $\omega_r(k)$ are the exact values at time k , and defining R_s , L_s and ψ_m are actual parameters and R_{sc} , L_{sc} and ψ_{sc} are the parameters that are only used in the predictive controller. According to (5) and (6), the current prediction error Δi_{sd} and Δi_{sq} can be expressed as:

$$\begin{aligned} \Delta i_{sd} &= |i_{sd}(k+1) - i_{sd}(k+1)| \\ &= T_s \left| \left(\frac{R_{sc}}{L_{sc}} - \frac{R_s}{L_s} \right) i_{sd}(k) + \left(\frac{1}{L_s} - \frac{1}{L_{sc}} \right) u_{sd} \right| \end{aligned} \quad (12)$$

$$\begin{aligned} \Delta i_{sq} &= |i_{sq}(k+1) - i_{sq}(k+1)| \\ &= T_s \left| \left(\frac{R_{sc}}{L_{sc}} - \frac{R_s}{L_s} \right) i_{sq}(k) + (\psi_{mc} - \psi_m) \omega_r(k) + \left(\frac{1}{L_s} - \frac{1}{L_{sc}} \right) u_{sq} \right| \end{aligned} \quad (13)$$

For the predictive errors due to different stator resistance mismatch, waveforms of d-axis and q-axis currents have similar tendencies, and the errors of the q-axis current as typical examples are shown in Fig. 1(a) - (d). As shown in the figures, the waveforms with different stator resistance and induction mismatches in Fig. 1 (a) and (b) have decreasing tendencies by $L_{sc}/L_s < 1$ and increasing $\lg(R_{sc}/R_s)$, and have increasing tendencies by $L_{sc}/L_s \geq 1$ and increasing $\lg(R_{sc}/R_s)$. The changing tendencies are became more obvious when the $\lg(R_{sc}/R_s)$ is larger than 0. The waveforms with different stator resistance and magnet flux mismatches are shown in Fig. 1(c) and enlarged around to zero mismatches are shown

in Fig. 1(d). The predictive errors decrease to zero at first and multiply towards infinity later, and these errors with larger magnet flux and less stator mismatches are reached to zero error quickly, and vice versa.

For the predictive errors due to different stator induction mismatch, the predictive errors of q-axis current with stator resistance and flux magnet mismatches are selected as typical examples, and these waves decrease to zero at first and increase slightly by increasing $\lg(L_{sc}/L_s)$ later which are shown in Fig. 1(e) – (h). The waveforms with same absolute values of R_{sc}/R_s-1 have similar changing tendencies and the same minimal errors in Fig. 1(e) and (f), and these waveforms have complete overlap in Fig. 1(g) and (h).

For the magnet flux mismatch, the predictive errors of d-axis and q-axis have different tendencies with stator resistance and induction mismatches which are shown in Fig. 1(i) – (l).

The predictive errors for the d-axis current are constant values by increasing $\lg(\psi_{mc}/\psi_m)$. The changing range of predictive error with $L_{sc}/L_s < 1$ is larger than the one with $L_{sc}/L_s \geq 1$, and predictive errors with same absolute values of R_{sc}/R_s-1 are same exactly. The predictive errors for the q-axis current with different stator induction mismatches are decreased by the conditions of $L_{sc}/L_s < 1$ and growing up $\lg(\psi_{mc}/\psi_m)$, and increased by the conditions of $L_{sc}/L_s \geq 1$ and growing up $\lg(\psi_{mc}/\psi_m)$. The predictive errors for the q-axis current with different stator resistance mismatches decrease at first and increase multiplied later when $R_{sc}/R_s \leq 1$, and continued to grow like exponential functions when $R_{sc}/R_s > 1$.

Compared with the stator resistance mismatch, the stator induction mismatch has the maximal sensitivity of the predictive error of the stator currents, and the flux magnet mismatch has the minimal sensitivity.

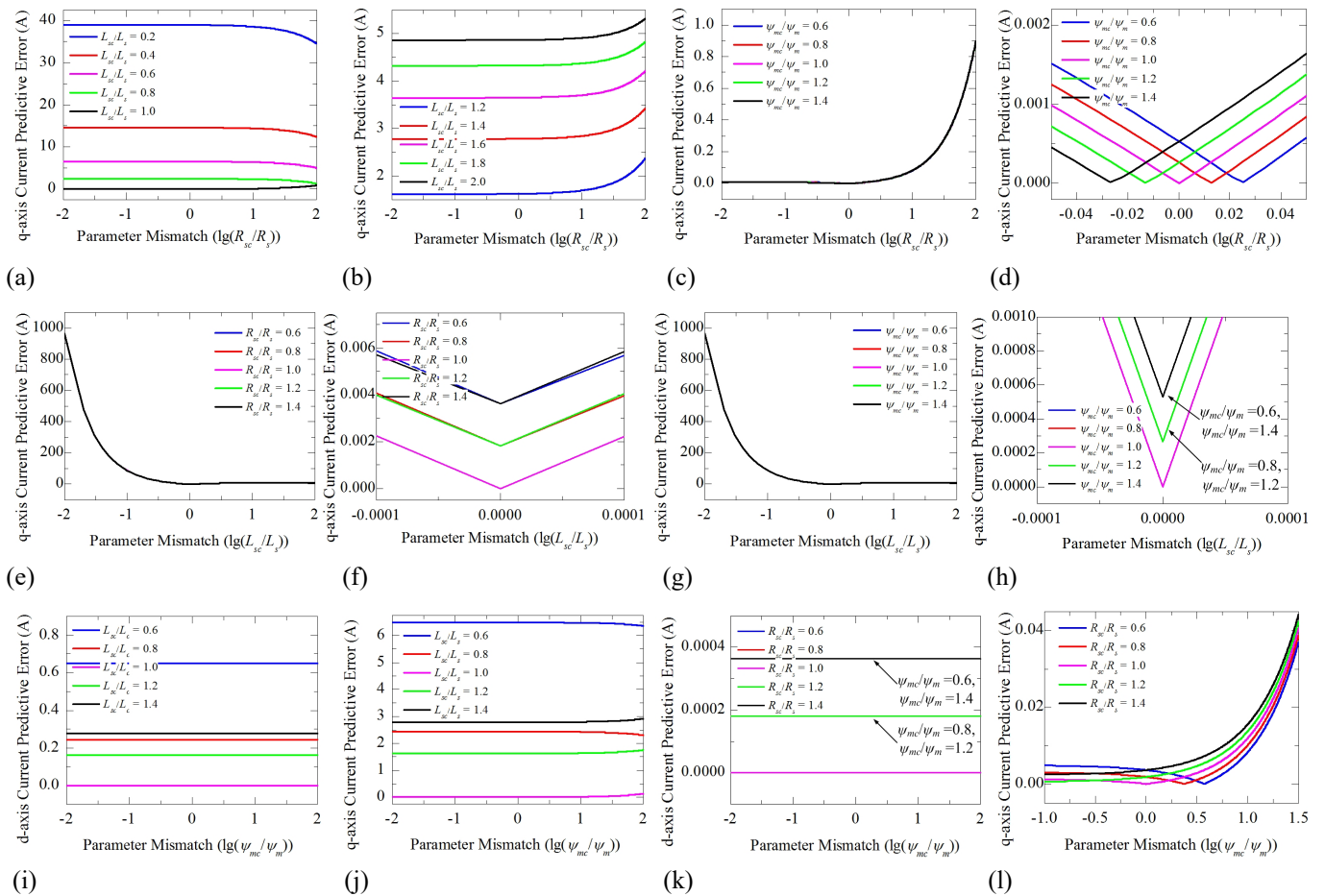


Fig. 1. Predictive error with parameter mismatches. (a) q-axis current predictive error with parameter mismatch $\lg(R_{sc}/R_s)$ and $L_{sc}/L_s \leq 1$, (b) q-axis current predictive error with parameter mismatch $\lg(R_{sc}/R_s)$ and $L_{sc}/L_s > 1$, (c) q-axis current predictive error with parameter mismatch $\lg(\psi_{mc}/\psi_m)$, (d) enlarged q-axis current predictive error with parameter mismatch $\lg(\psi_{mc}/\psi_m)$, (e) q-axis current predictive error with parameter mismatch $\lg(L_{sc}/L_s)$ and R_{sc}/R_s , (f) enlarged q-axis current predictive error with parameter mismatch $\lg(L_{sc}/L_s)$ and R_{sc}/R_s , (g) q-axis current predictive error with parameter mismatch $\lg(L_{sc}/L_s)$ and ψ_{mc}/ψ_m , (h) enlarged q-axis current predictive error with parameter mismatch $\lg(L_{sc}/L_s)$ and ψ_{mc}/ψ_m , (i) d-axis current predictive error with parameter mismatch $\lg(\psi_{mc}/\psi_m)$ and L_{sc}/L_s , (j) q-axis current predictive error with parameter mismatch $\lg(\psi_{mc}/\psi_m)$ and L_{sc}/L_s , (k) d-axis current predictive error with parameter mismatch $\lg(\psi_{mc}/\psi_m)$ and R_{sc}/R_s , (l) q-axis current predictive error with parameter mismatch $\lg(\psi_{mc}/\psi_m)$ and R_{sc}/R_s .

3. PROPOSED METHOD

3.1 Basic Principle

The predictive current error is unavoidable due to the parameter mismatches in the PI-MPCC method. Moreover, the ADR-/LADR-structure can replace the PI controller to obtain the predictive current error compensation with suitable system dynamics. The structure of the proposed LADR-SS-MPCC is shown in Fig. 2, where the PD Combination block can be expressed as follow for a n-order controlled plant:

$$u_o = p_1(r - z_1) - k_{d1}z_2 - \dots - k_{dn-1}z_n \quad (14)$$

where r is reference signal, p_1 is proportional coefficient, k_{dj} ($j=1,2,\dots,n-1$) are derivational coefficient.

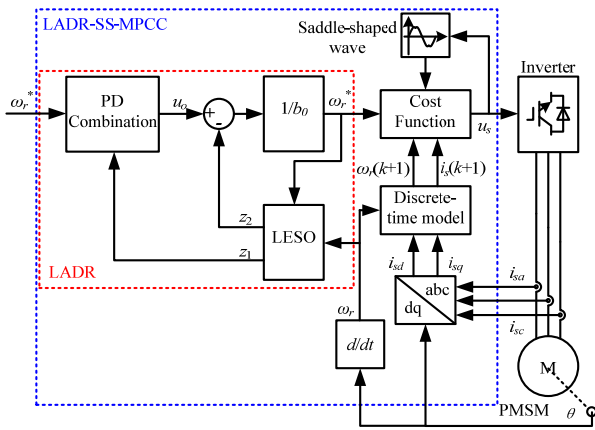


Fig. 2. Structure of the proposed method.

3.2 LADR-structure Frequency Domain Tuning Method

For PI-MPCC, the PI speed controller can be tuned in the frequency-domain, and the close-loop transfer function of the MPCC can be seen as 1 because the bandwidth of the MPCC is always high enough compared with the PI speed controller corner frequency ω_{sc} . Therefore, two parameters of the PI speed controller have a tuning method in the frequency-domain which can be expressed as:

$$K_{sp} = \frac{J\omega_{sc}}{p\psi_m} \quad (15)$$

$$K_{si} \leq \frac{\omega_{sc}}{5} K_{sp} \quad (16)$$

The controlled plant of the speed controller can be simplified as a 1-order transfer function:

$$\omega_r(s) = \frac{p\psi_m}{Js} i_{sq}^*(s) \quad (17)$$

and the order of the LADR-structure with reduced order LESO can be selected as 1, and the LESO and the LSEF can be expressed as:

$$\begin{cases} \dot{z}_1 = z_2 - \beta_1(z_1 - y) + b_0 u \\ \dot{z}_2 = -\beta_2(z_1 - y) \end{cases} \quad (18)$$

$$u = \frac{1}{b_0}(-z_2 + u_o) \quad (19)$$

where

$$u_o = p_1(\omega_r^* - z_1) \quad (20)$$

and β_1 and β_2 are positive adjustable coefficients in the LESO, and p_1 and b_0 are positive variables in the PD combination and LSEF.

Based on the obtaining results of the PI controller in (15) and (16), an expression can be selected to tune the coefficients of the 1-order LADR- structure:

$$\alpha_0^3 + |b_0|K_{sp}\alpha_0 - |b_0|K_{si} = 0 \quad (21)$$

where the middle-variable $\alpha_0 = \beta_2/\beta_1$, and α_0 can be obtained by the Cardano's formula if b_0 is selected.

The parameter p_1 can be obtained by the expression as:

$$p_1 = \frac{|b_0|}{\alpha_0} K_{si} \quad (22)$$

and the stability of the system can be ensured by a suitable coefficient β_1 .

In this paper, parameters K_{sp} and K_{si} of the PI speed controller are select as 0.00602 and 0.3042 respectively according to (B. Kou et al., 2008), and the corner frequency ω_{sc} and variable b_0 are selected as 100 rad/s and 88711, and the β_1 and β_2 are calculated as 2×10^5 and 4×10^8 . The pole/zero map of the LADR-structure with the controlled plant is shown in Fig. 3. The system is stable because all of the poles and zeros are located at the left half of the complex plane.

3.3 Saddle-shaped Wave Digital Realization and Influence

3.3.1 Analysis and Digital Realization

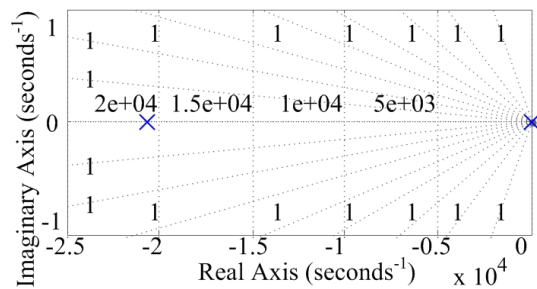


Fig. 3. Pole/zero map of the LADR-structure.

The expressions of the positive half-cycle of saddle-shaped waveform in Fig. 4(a) and its odd prolongation are:

$$f(\omega t) = \begin{cases} \sqrt{3} \sin(\omega t) & 0 \leq \omega t < \frac{\pi}{6}, \frac{5\pi}{6} \leq \omega t \leq \pi \\ \sin\left(\omega t + \frac{\pi}{6}\right) & \frac{\pi}{6} \leq \omega t < \frac{\pi}{2} \\ \sin\left(\omega t - \frac{\pi}{6}\right) & \frac{\pi}{2} \leq \omega t < \frac{5\pi}{6} \end{cases} \quad (23)$$

$$f(\omega t) = \frac{2}{\sqrt{3}} \sin(\omega t) + \frac{3}{4} \times \frac{2}{\pi} \sum_{m=1}^{\infty} (-1)^{m-1} \frac{\sin[(6m-3)\omega t]}{(3m-1)(3m-2)} \quad (24)$$

$$= \frac{2}{\sqrt{3}} \sin(\omega t) + \frac{3}{2\pi} \left[\frac{1}{2} \sin(3\omega t) - \frac{1}{4 \times 5} \sin(9\omega t) + \dots \right]$$

It can be seen that only zero-sequence component of the 3-order and its odd times order harmonics are contained in the saddle-shaped waveform.

Besides, a kind of crossing and interrupting waveform for the three-phase sinusoidal waves is shown in Fig. 4(b), and the waveform and its odd prolongation are expressed as (J. Lyu et al., 2016):

$$h(\omega t) = \begin{cases} \sin(\omega t) & 0 \leq \omega t < \frac{\pi}{6} \\ \sin\left(\omega t + \frac{2\pi}{3}\right) & \frac{\pi}{6} \leq \omega t \leq \frac{\pi}{3} \end{cases} \quad (25)$$

$$h(\omega t) = \frac{3\sqrt{3}}{2\pi} \left[\frac{1}{2} \sin(3\omega t) - \frac{1}{20} \sin(9\omega t) + \dots \right] \quad (26)$$

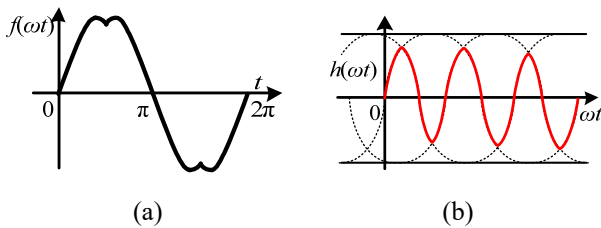


Fig. 4. Waveforms of saddle-shaped method. (a) Saddle-shaped waveform, (b) Crossing and interrupting waveform.

Compared with (24) and (26), the saddle-shaped waveform can be generated by a proportional coefficient k' based on the three-phase sinusoidal waves. A digital realization method for the PMSM circuit structure is shown in Fig. 5, and the saddle-shaped waveform can be obtained by the total of the maximal and the minimal values of the predictive voltages in (10) and (11) on the abc coordinate.

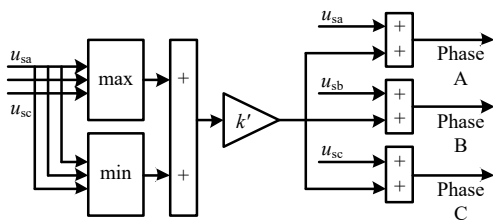


Fig. 5. Digital realization method.

3.3.2 Torque Ripple Analysis

For the inserted harmonic currents above-mentioned, the 3-order and its odd times order harmonics have no any accesses in the PMSM circuit structure, and the stator current harmonics have no any 3-order and its integral-times order harmonics because the connection type of the PMSM stator is always selected as Y-type. According to (L. Li et al., 2018), the stator currents on the abc coordinate only include $6n \pm 1$ ($n = 1, 2, 3, \dots$) orders harmonics, and can be expressed as:

$$i_{sa} = i_1 \cos(\omega t + \theta_1) + i_5 \cos(\omega t + \theta_5) + i_7 \cos(\omega t + \theta_7) + \dots \quad (27)$$

$$i_{sb} =$$

$$i_1 \cos\left(\omega t + \theta_1 - \frac{2\pi}{3}\right) + i_5 \cos\left(\omega t + \theta_5 - \frac{2\pi}{3}\right) + i_7 \cos\left(\omega t + \theta_7 - \frac{2\pi}{3}\right) + \dots \quad (28)$$

$$i_{sc} =$$

$$i_1 \cos\left(\omega t + \theta_1 + \frac{2\pi}{3}\right) + i_5 \cos\left(\omega t + \theta_5 + \frac{2\pi}{3}\right) + i_7 \cos\left(\omega t + \theta_7 + \frac{2\pi}{3}\right) + \dots \quad (29)$$

The electromagnetic torque due to the harmonic currents can be expressed as:

$$T_{eh} = \frac{1}{\omega_r} (e_a i_{sa} + e_b i_{sb} + e_c i_{sc}) \quad (30)$$

$$= T_0 + T_6 \cos(6p\omega_r t) + T_{12} \cos(12p\omega_r t) + \dots$$

where the e_a , e_b and e_c are the three-phase electromotive forces (EMFs), and the T_0 , T_6 and T_{12} are the amplitudes of the average torque, the 6-order harmonic torque and the 12-order harmonic torque which can be expressed as:

$$T_0 = \frac{3}{2\omega_r} (E_{m1} I_{m1} + E_{m5} I_{m5} + E_{m7} I_{m7} + \dots) \quad (31)$$

$$T_6 =$$

$$\frac{3}{2\omega_r} [(E_{m7} - E_{m5}) I_{m1} + (E_{m11} - E_{m1}) I_{m5} + (E_{m13} + E_{m1}) I_{m7} + \dots] \quad (32)$$

$$T_{12} =$$

$$\frac{3}{2\omega_r} [(E_{m13} - E_{m11}) I_{m1} + (E_{m17} - E_{m7}) I_{m5} + (E_{m19} + E_{m5}) I_{m7} + \dots] \quad (33)$$

where E_{m1} and I_{m1} are the amplitudes of the fundamental EMFs and stator currents, and $E_{m(6n \pm 1)}$ and $I_{m(6n \pm 1)}$ are the amplitudes of the different order of harmonics EMFs and stator currents. The stator currents of the proposed method are same as (27) – (29), and the inserted harmonic currents will not bring any extra-ripples for the electromagnetic torque T_e .

4. SIMULATION IMPLEMENTATION AND RESULTS

Simulation studies are carried out on the MATLAB/simulink software based on the structure in Fig. 2, and the main parameters of the simulations are listed in Tab. 1.

Table 1. Units for Parameters.

Symbol	Quantity	Value
R_s	Stator resistance	2.875Ω
L_s	Stator self-inductance	0.835mH
J	Rotor inertia	0.0008kg.m ²
B	Friction coefficient	0.0008N.m.s
p	The number of pole pairs	4
ψ_m	Flux magnitude due to the rotor magnets	0.175Wb

The speed reference and actual speed waveforms with different control methods are shown in the Fig. 6 where the

parameters of the PI-MPCC are tuned by the frequency-domain method in (B. Kou et al., 2008), and the A-phase stator current for the proposed method is shown in Fig. 7. The reference signal is changed from 1000 to 800 at 0.25s, and the load torque is changed from 2 N.m to 3 N.m at 0.45s. As shown in the figure, the LADR-MPCC and the PI-MPCC methods can track the reference in 0.001s and 0.09s at 0.25s, and resist the disturbance in 0.005s and 0.13s respectively. The rapidity and overshoot of the proposed method are improved about 96.154% and 91.643% respectively during the resisting process at 0.45s, and the dynamics has an obvious improvement compared with the PI-MPCC method.

A group of dynamic comparison among the proposed method, the LADR-MPCC method and the PI-MPCC method are listed in Tab. 2. As shown in the table, the proposed method has similar dynamics during resisting process, and the settling times and overshoots during tracking processes are improved about 25% and 72.251% respectively compared with the LADR-MPCC method. However, the ITAE of the proposed method is larger than the LADR-MPCC method about 17.614% due to larger overshoot and a little weakened dynamics during the resisting process of the proposed method compared with the LADR-MPCC method.

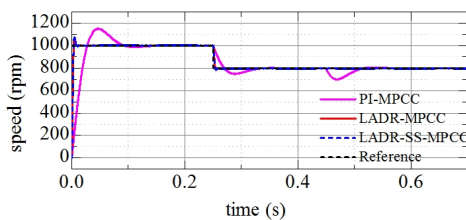


Fig. 6. Speed waveforms with different control methods.

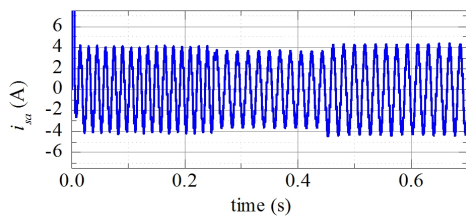


Fig. 7. A-phase stator current waveform for the proposed method.

Table 2. Performances Comparison.

Control Performances	LADR-SS-MPCC	ADRC-MPCC	PI-MPCC
Settling time at start	0.008s	0.012s	0.16s
Settling time at 0.25s	0.002s	0.008s	0.09s
Settling time at 0.45s	0.005s	0.005s	0.13s
Overshoot at start	1.808%	7.293%	14.908%
Overshoot at 0.25s	0.743%	1.900%	6.121%
Overshoot at 0.45s	1.030%	0.976%	12.325%
Speed ITAE in 0.8s	0.2498	0.2058	3.382

The inserted 3-order and its odd-times order harmonics waveform and the saddle-shaped waveform are shown in the Fig. 8. The waveforms are almost flooded by harmonics above-mentioned and observed rough shapes which are conform to the waves in Fig. 4 by the envelopes of the waves.

However, the harmonics of the LADR-MPCC strategy are distributed evenly throughout the testing range which generates large ripples of the electromagnetic torque T_e due to the variable switching frequency. According to the Fourier analysis results of the stator currents of the proposed method and the PI-MPCC method in the Fig. 9, the orders of harmonics are same and the amplitudes of harmonics are decreased because some specific orders of harmonics are offset (J. Lyu et al., 2016).

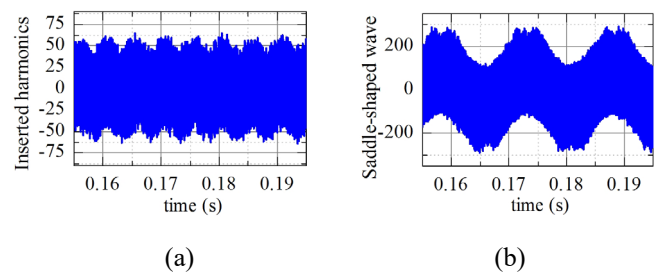


Fig. 8. Waveforms of inserted and saddle-shaped method. (a) Inserted 3-order and its odd-times order harmonics, (b) Saddle-shaped waveform.

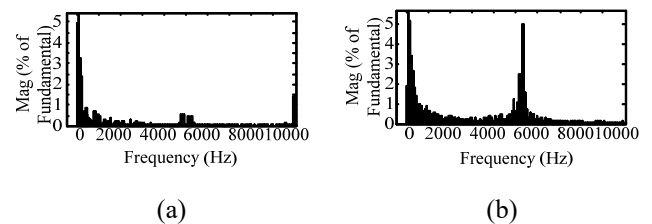


Fig. 9. Fourier analysis results for the stator current. (a) LADR-SS-MPCC, (b) PI-MPCC.

The mismatched stator resistance R_{sc} , stator induction L_{sc} and magnet flux ψ_{mc} are linearly increased in every sampling period. Fig. 10 provides the parameter variation ranges that ensure the PMSM system operates stable for the PI-MPCC and the LADR-SS-MPCC. It can be seen that stator current and speed under the LADR-SS-MPCC are stable during the testing range, whereas speed under PI-MPCC will be unstable when R_{sc} decreases to about 41.739% or ψ_{mc} decreases to about 68.571%. The lower bound of the stator induction variation range to guarantee control system stability is 11.976% for the LADR-SS-MPCC, and 95.808% for the PI-MPCC. In the LADR-SS-MPCC, the predictive error caused by the mismatched parameters can be estimated by the LESO of LADR-structure and compensated for the SS-MPCC with lower harmonic amplitudes. The proposed method has better robustness compared with the PI-MPCC, and compensation of the predictive error also improves the dynamics and steady-state performances.

5. EXPERIMENTAL RESULTS

The proposed LADR-SS-MPCC method is verified on the experimental platform illustrated in Fig. 11. The platform mainly consists of a 1kW PMSM (INOVANCE ISMH2-10C30CD) with an incremental encoder (INOVANCE EI34H), a three-phase inverter with IGBTs (FGL35N120FTD) and a DSP (TMS320F2812PGFA) with a CLPD (EPM240T100I5N) control system. The algorithm proposed in this paper is implemented in the DSP with CPLD system, and the load torque is provided by a dynamometer and displayed by an oscilloscope.

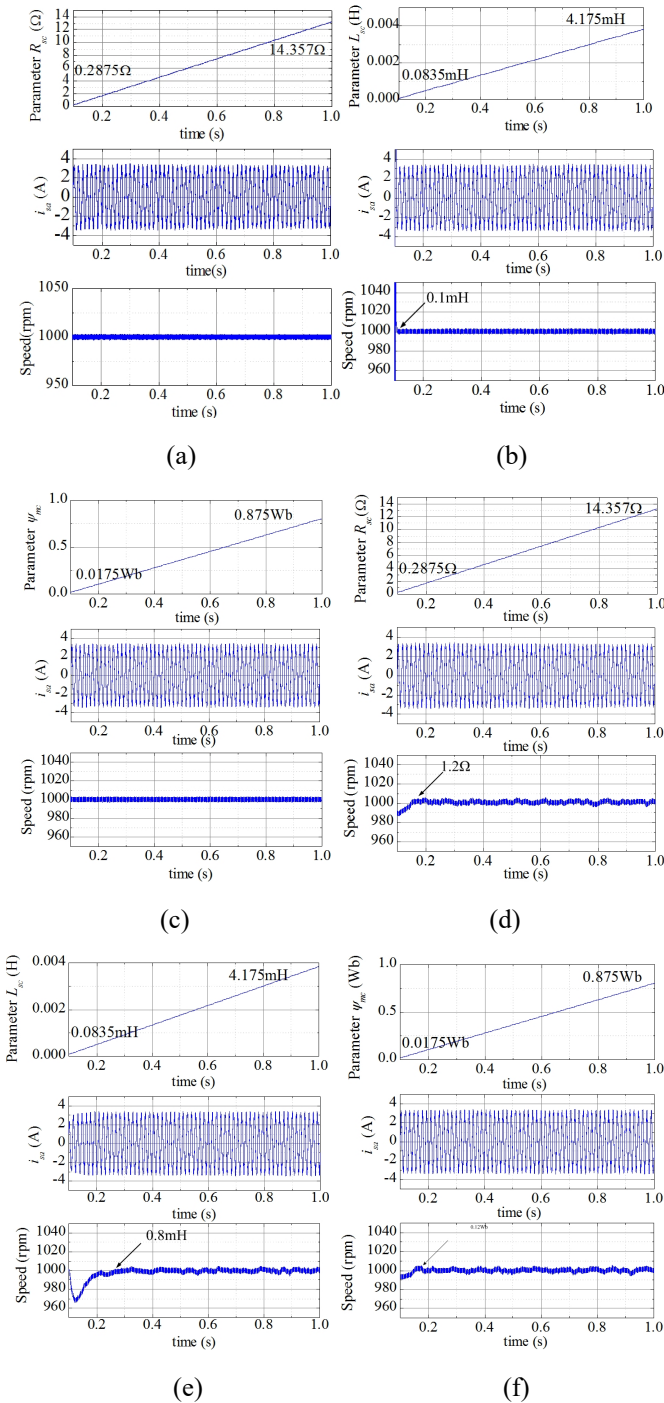


Fig. 10. Waveforms of the A-phase current and speed with different parameter mismatches. (a) LADR-SS-MPCC with

R_s mismatch, (b) LADR-SS-MPCC with L_s mismatch, (c) LADR-SS-MPCC with ψ_m mismatch, (d) PI-MPCC with R_s mismatch, (e) PI-MPCC with L_s mismatch, (f) PI-MPCC with ψ_m mismatch.

The reference is selected as 500rpm at start. The speed, A-phase stator current and load torque waveforms are shown in Fig. 12(a), and the inserted harmonics and saddle-shaped waveforms are shown in Fig. 12(b). As shown in the figures, the speed can track the reference in the steady state with ripple about 1.534% and load torque 2 N.m, and the inserted harmonics and the saddle-shaped waves are more similar to the ideal waves in Fig. 4 compared with the simulations.

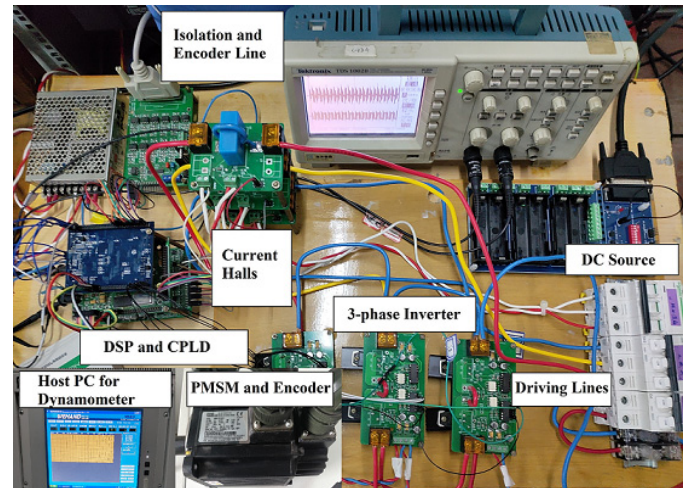


Fig. 11. Test bench for evaluations.

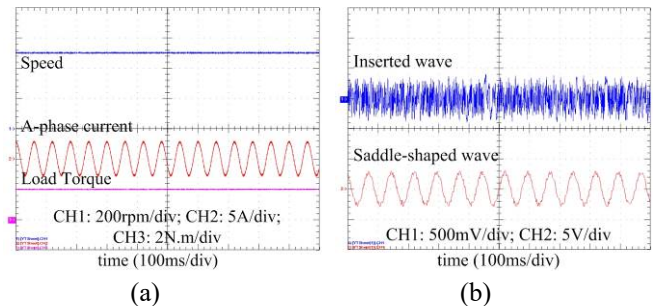


Fig. 12. Steady state experimental waveforms of LADR-SS-MPCC method. (a) Speed, current and load torque waveforms, (b) Inserted harmonics and saddle-shaped waveforms.

The reference is changed to 400rpm and the load torque is changed to 2.2 N.m respectively when the system operates in the steady state. The waveforms of the proposed method during transient processes are shown in Fig. 13, and waveforms of the PI-MPCC method are shown in Fig. 14. Under same conditions, the proposed method can track the reference in about 20ms and resist the disturbance with almost little transient process, and the PI-MPCC method also can track the reference in about 260ms and resist the disturbance in about 280ms with some obvious overshoots. The dynamics of the proposed method is improved clearly by the comparison of LADR-structure.

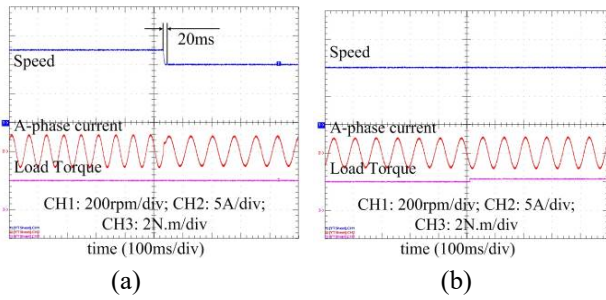


Fig. 13. Experimental waveforms of LADR-SS-MPCC method. (a) Reference step change, (b) Load torque step change.

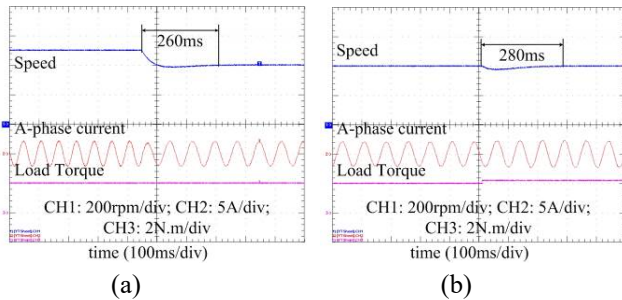


Fig. 14. Experimental waveforms of PI-MPCC method. (a) Reference step change, (b) Load torque step change.

The compensation of the predictive error is estimated, and the parameter sensitivities and its boundaries are further determined by the experimental platform more accurately. The stator resistance, induction and magnet flux variation ranges are shown in Fig. 15 - 17, and boundaries are 0.1% - 901.7%, 11.01% - 2000%, and 0.001% - 5000% respectively to ensure stable operation.

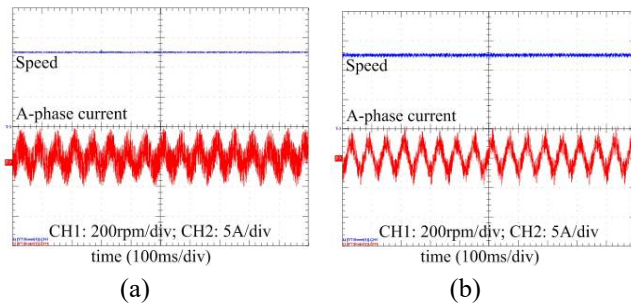


Fig. 15. Experimental waveforms of the proposed method with stator resistance mismatch. (a) Upper bound at 901.7%, (b) Lower bound at 0.1%.

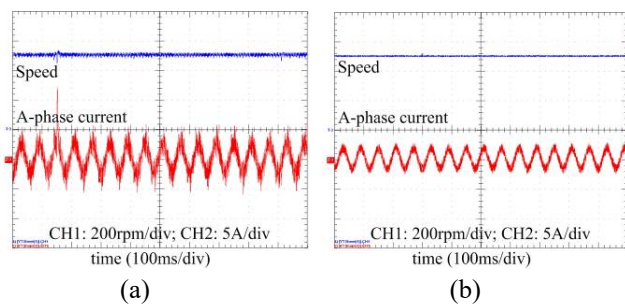


Fig. 16. Experimental waveforms of the proposed method with stator induction mismatch. (a) Upper bound at 2000%, (b) Lower bound at 11.01%.

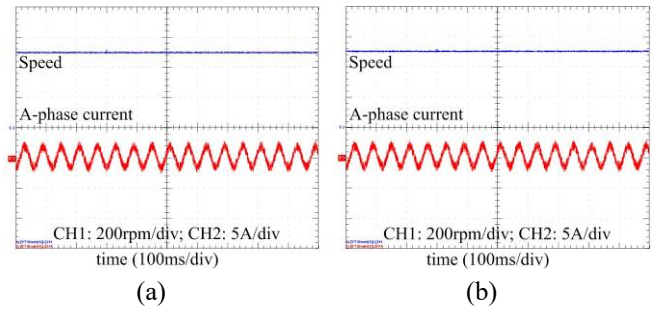


Fig. 17. Experimental waveforms of the proposed method with magnet flux mismatch. (a) Upper bound 5000%, (b) Lower bound at 0.001%.

6. CONCLUSIONS

A LADR-SS-MPCC has been studied in this paper for the PMSM control system. Based on the analysis of the predictive error of the parameter mismatches and the frequency-domain tuning method of the LADR-structure, the proposed method shows that the performances including dynamics, parameter sensitivities and harmonics are mainly more effective than the PI-MPCC and the LADR-MPCC strategies. The advantages of the proposed method have been demonstrated by the analysis of simulation and experimental results.

Compared with the PI-MPCC, the parameter sensitivities of the stator resistance, induction and magnet flux for the proposed method are improved about 6.486%, 17.178% and 11.953%, and the settling times of tracking reference and resisting disturbance are decreased about 97.778% and 96.154% respectively which are similar with the LADR-MPCC strategy. Moreover, the amplitudes of the stator current harmonic with some special orders decrease due to the saddle-shaped waveform in the proposed method, and will not bring any extra-ripples in the torque compared with the PI-MPCC method.

REFERENCES

- B. Kou and S. Cheng (2008). *AC Servo Motor and Control*, 1st ed. Beijing, China: China Machine Press, pp. 62-77.
- B. Kou, F. Xing, C. Zhang, et al (2016). Improved ADRC for a Maglev Planar Motor with a Concentric Winding Structure. *Applied Sciences*, volume (6), pp. 419-433.
- B. Wang, X. Chen, Y. Yu, et al (2017). Robust Predictive Current Control With Online Disturbance Estimation for Induction Machine Drives. *IEEE Trans. Power Electron.*, volume(32), pp. 4663-4674.
- B. Wang, Z. Dong, Y. Yu, et al (2020). Static-Errorless Deadbeat Predictive Current Control Using Second-Order Sliding-Mode Disturbance Observer for Induction Machine Drives. *IEEE Trans. Power Electron.*, volume(33), pp. 2395-2403.
- C. Liu, G. Luo, Z. Chen, et al (2020). Measurement delay compensated LADRC based current controller design for PMSM drives with a simple parameter tuning method. *ISA Transaction*, volume(101), pp. 482-492.
- C. Zheng, T. Dragicevic, Z. Zhang, et al (2020). Model Predictive Control of LC-Filtered Voltage Source

- Inverters With Optimal Switching Sequence. *IEEE Trans. Power Electron. (Early Access)*.
- F. Wang, J. Wang, R. M. Kennel, et al (2019). Fast Speed Control of AC Machine Without the Proportional-Integral Controller: Using an Extended High-Gain State Observer. *IEEE Trans. Power Electron.*, volume(34), pp. 9006-9015.
- F. Wang, S. A. Davari, Z. Chen, et al (2017). Finite Control Set Model Predictive Torque Control of Induction Machine With a Robust Adaptive Observer. *IEEE Trans. Ind. Electron.*, volume(64), pp. 2631-2641.
- F. Wang, Z. Zhang, S. A. Davari, et al (2017). An Encoderless Predictive Torque Control for an Induction Machine With a Revised Prediction Model and EFOSMO. *IEEE Trans. Ind. Electron.*, volume(64), pp. 6287-6298.
- J. Li, Y. Xia, X. Qi, et al (2017). On the Necessity, Scheme, and Basis of the Linear-Nonlinear Switching in Active Disturbance Rejection Control. *IEEE Trans. Ind. Electron.*, volume(64), pp. 1425-1435.
- J. Lyu, W. Hu, F. Wu, et al (2016). Three-level saddle space vector pulse width modulation strategy based on two-level space vector pulse width modulation for neutral-point-clamped three-level inverters. *IET Power Electronics*, volume(9), pp. 874-882.
- J. Rodriguez and P. Cortes (2012). *Predictive Control of Power Converters and Electrical Drives*. 1st ed. Chichester, U.K.: IEEE Press-Wiley, pp. 133-144.
- L. Li, K. M. Lee, K. Bai, et al (2018). Inverse Models and Harmonics Compensation for Suppressing Torque Ripples of Multiphase Permanent Magnet Motor. *IEEE Trans. Ind. Electron.*, volume(65), pp. 8730-8739.
- L. Yan, F. Wang, M. Dou, et al (2020). Active Disturbance-Rejection-Based Speed Control in Model Predictive Control for Induction Machines. *IEEE Trans. Ind. Electron.*, volume(67), pp. 2574-2574.
- M. Habibullah, D. D. Lu, D. Xiao, et al (2017). Finite-State Predictive Torque Control of Induction Motor Supplied from a Three-Level NPC Voltage Source Inverter. *IEEE Trans. Power Electron.*, volume(32), pp. 479-489.
- M. Zareian and M. H. Shafiei (2020). A modification in the structure of low-power high-gain observers to improve the performance in the presence of disturbances and measurement noise. *European Journal of Control*, volume(Available online 31), pp. 1-11.
- Q. Wang, G. Wang, N. Zhao, et al (2020). An Impedance Model Based Multi-Parameter Identification Method of PMSM for Both Offline and Online Conditions. *IEEE Trans. Power Electron. (Early Access)*.
- S. Siami, D. A. Khaburi and J. Rodriguez (2017). Torque Ripple Reduction of Predictive Torque Control for PMSM Drives With Parameter Mismatch. *IEEE Trans. Power Electron.*, volume(32), pp. 7160-7168.
- T. Englert and K. Graichen(2018). Nonlinear model predictive torque control of PMSMs for high performance applications. *Control Engineering Practice*, volume(81), pp. 43-54.
- T. Geyer(2013). Model Predictive Direct Torque Control: Derivation and Analysis of the State-feedback Control Law. *IEEE Trans. Ind. Appl.*, volume(49), pp. 2146-2157.
- T. Geyer(2016). *Model predictive control of high power converters and industrial drives*, 1st ed. Chichester, U.K.: Wiley, pp. 29-76.
- T. Sun, R. Yang, H. Li, et al (2020). Active Motor Rotor Temperature Management Based on One-Node Thermal Network Model Predictive Control. *IEEE Trans. Power Electron.*, volume(35), pp. 11213-11221.
- X. Yuan, S. Zhang and C. Zhang (2020). Improved Model Predictive Current Control for SPMSM Drives With Parameter Mismatch. *IEEE Trans. Ind. Electron.*, volume(67), pp. 852-862.
- Y. Wei, Y. Wei, Y. Sun, et al (2020). Prediction Horizons Optimized Nonlinear Predictive Control for PMSM Position System. *IEEE Trans. Ind. Electron.*, volume(67), pp. 9153-9163.
- Y. Zhang, B. Zhang, H. Yang, et al (2019). Generalized Sequential Model Predictive Control of IM Drives With Field-Weakening Ability. *IEEE Trans. Power Electron.*, volume(34), pp. 8944-8955.
- Z. Zhang, F. Wang, J. Wang, et al (2017). Nonlinear Direct Control for Three-Level NPC Back-to-Back Converter PMSG Wind Turbine Systems: Experimental Assessment With FPGA. *IEEE Trans. Ind. Inform.*, volume(13), pp. 1172-1183.
- Z. Zou and Y. Liu (2019). Simulation Calculation of the Magnetic Torque of Dual Mode Permanent Magnet Transmission Based on Magnetic Circuit Analysis. *IEEE Access*, volume(7), pp. 149926-149934.